JACS
JOURNAL OF THE AMERICAN CHEMICAL SOCIETY
Article
pubs.acs.org/JACS

Chiral Redox-Active Isosceles Triangles

Siva Krishna Mohan Nalluri,[†] Zhichang Liu,[†] Yilei Wu,[†,‡] Keith R. Hermann,[†] Avik Samanta,[†] Dong Jun Kim,[†] Matthew D. Krzyaniak,[†,‡] Michael R. Wasielewski,[†,‡] and J. Fraser Stoddart*[,†]

[†]Department of Chemistry and [‡]Argonne-Northwestern Solar Energy Research (ANSER) Center, Northwestern University, 2145 Sheridan Road, Evanston, Illinois 60208-3113, United States

Supporting Information

ABSTRACT: Designing small-molecule organic redox-active materials, with potential applications in energy storage, has received considerable interest of late. Herein, we report on the synthesis, characterization, and application of two rigid chiral triangles, each of which consist of non-identical pyromellitic diimide (PMDI) and naphthalene diimide (NDI)-based redox-active units. ^{1}H and ^{13}C NMR spectroscopic investigations in solution confirm the lower symmetry (C_2 point group) associated with these two isosceles triangles. Single-crystal X-ray diffraction analyses reveal their rigid triangular prism-like geometries. Unlike previously investigated equilateral triangle containing three identical NDI subunits, both isosceles triangles do not choose to form one-dimensional supramolecular nanotubes by dint of [C−H···O] interaction-driven columnar stacking. The rigid isosceles triangle, composed of one NDI and two PMDI subunits, forms—in the presence of *N,N*-dimethylformamide—two different types of intermolecular NDI−NDI and NDI−PMDI $\pi-\pi$ stacked dimers with opposite helicities in the solid state. Cyclic voltammetry reveals that both isosceles triangles can accept reversibly up to six electrons. Continuous-wave electron paramagnetic resonance and electron−nuclear double-resonance spectroscopic investigations, supported by density functional theory calculations, on the single-electron reduced radical anions of the isosceles triangles confirm the selective sharing of unpaired electrons among adjacent redox-active NDI subunit(s) within both molecules. The isosceles triangles have been employed as electrode-active materials in organic rechargeable lithium-ion batteries. The evaluation of the structure−performance relationships of this series of diimide-based triangles reveals that the increase in the number of NDI subunits, replacing PMDI ones, within the molecules improves the electrochemical cell performance of the batteries.

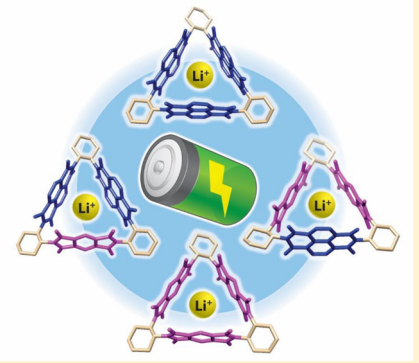

INTRODUCTION

Understanding of the geometrical constraints between multiple redox-active aromatic building blocks that exhibit efficient electron hopping and delocalization has presented a considerable challenge to those researchers fabricating[1−5] organic photovoltaic and molecular electronic devices. The efficiency of intra- as well as intermolecular charge mobilities in organic semiconductors relies[6] on maximizing electronic coupling and minimizing reorganizational energies associated with charge transport between neighboring π-conjugated redox-active units. These factors are determined, however, by (i) the relative orientations, (ii) the intermolecular distances, and (iii) the energy matches involving neighboring redox-active units.[7] In this context, a number of π-conjugated aromatic diimides, particularly pyromellitic diimides (PMDIs), naphthalene diimides (NDIs) and perylene diimides (PDIs), all of which exhibit unique redox characteristics, have been employed as n-type organic semiconductors with potential applications in organic field-effect transistors,[8−10] photovoltaics,[11] and energy storage devices,[12−14] including lithium- and sodium-ion batteries.[15] In particular, π-conjugated electron-deficient NDIs[16,17] have been investigated increasingly in a number of fields such as charge transport,[18,19] chemosensing,[20,21] synthetic membrane transport,[22,23] organocatalysis,[24,25] and biocatalytic charge-transfer assemblies.[26,27] Despite continued efforts relating to a number of π-conjugated redox-active molecules, the exact structure−performance relationship for efficient charge mobilities remains elusive.[28]

Recently, we reported[29] the synthesis of a chiral equilateral triangle (−)-**3NDI-Δ**, consisting of three redox-active NDI units that can accept reversibly up to six electrons. Both the experimental observations and theoretical calculations on (−)-**3NDI-Δ** reveal that a remarkable cyclical through-space electron delocalization occurs among the overlapping π-orbitals of the pairs of adjacent NDI units, as evidenced by the complete sharing of an unpaired electron in the stable radical anionic state of this equilateral triangle. Another important aspect of (−)-**3NDI-Δ** is the formation[30,31] of a supramolecular gel, composed of a dense network of entangled nanofibers, in (*E*)-1,2-dichloroethene, as well as by its solvent-dependent packing into a variety of solid-state superstructures—that is, the formation of (i) non-tubular superstructures in $CHCl_3$, (ii) single-handed helical tetrameric nanotubes in $ClCH_2CH_2Cl$, and (iii) rigid infinite non-helical nanotubes in $ClCH_2CH_2Br$, $ClCH_2CH_2I$, and $BrCH_2CH_2Br$—driven by the columnar

Received: February 24, 2016
Published: April 12, 2016

DOI: 10.1021/jacs.6b02086
J. Am. Chem. Soc. 2016, 138, 5968−5977

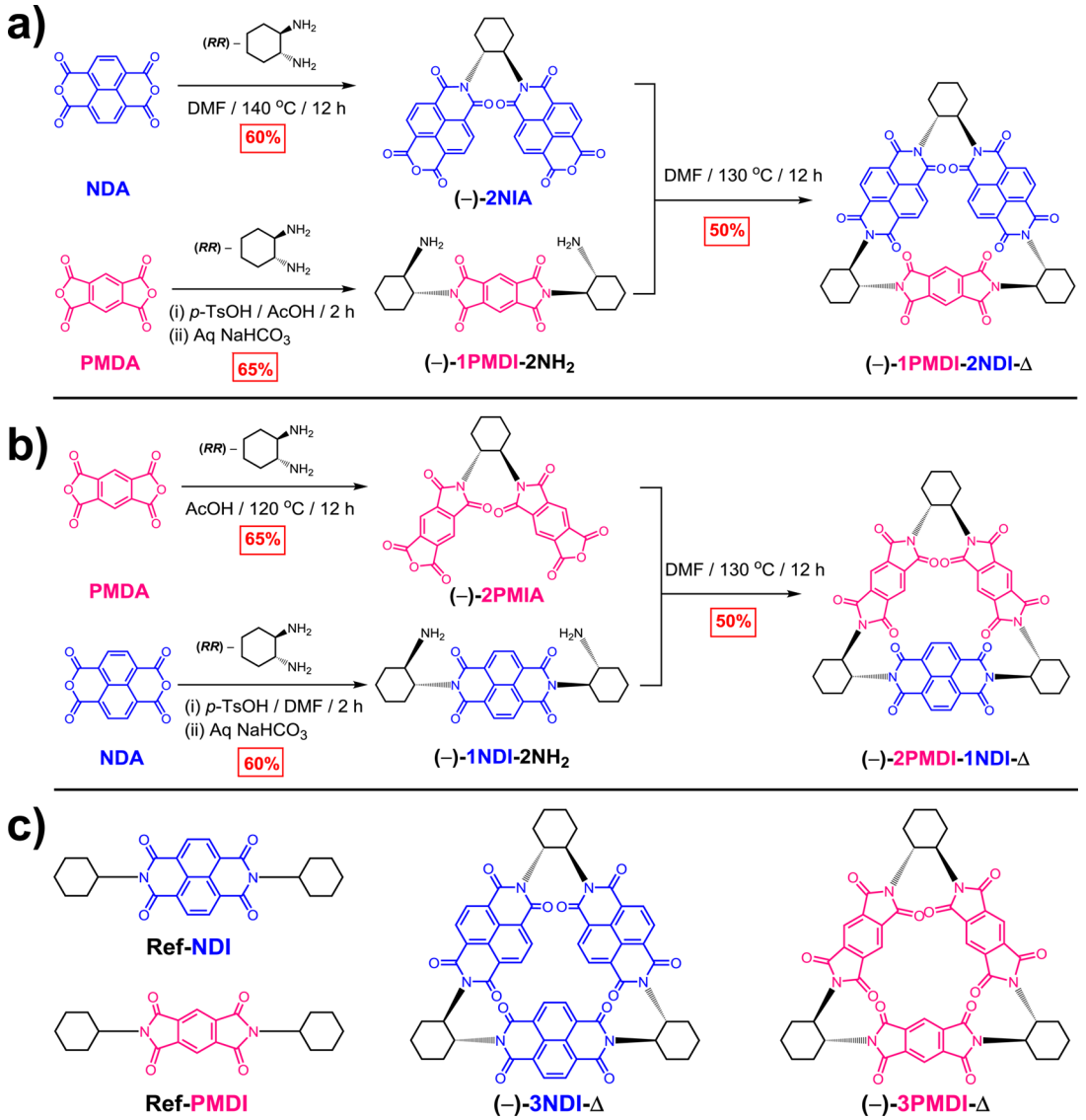

Figure 1. Stereospecific stepwise preparation of chiral isosceles triangles (a) (−)-**1PMDI-2NDI-Δ** and (b) (−)-**2PMDI-1NDI-Δ**, from (*RR*)-*trans*-1,2-cyclohexanediamine, naphthalenetetracarboxylic dianhydride (NDA), and pyromellitic dianhydride (PMDA). (c) Structural formulas of the monomeric reference compounds (**Ref-NDI** and **Ref-PMDI**) and the chiral equilateral triangles [(−)-**3NDI-Δ** and (−)-**3PMDI-Δ**]. The aromatic NDI and PMDI subunits within the molecular triangles are shown in blue and magenta, respectively.

stacking of (−)-**3NDI-Δ** with a 60° rotational angle between the neighboring triangles and employing multiple weak [C−H···O] interactions associated with directed halogen−halogen (X) interactions along the [X···X]-bonded solvent chains inside the nanotubes. In the meantime, Awaga[32] has reported the X-ray superstructure of the radical anion of (−)-**3NDI-Δ**, formed by electrochemical reduction, revealing the formation of an impressive K_4 structure, driven by the intermolecular $\pi-\pi$ stacking interactions of the NDI radical anions in the equilateral triangle. It should be emphasized that all of these observations are a consequence of three equivalent NDI units arranged in a shape-persistent triangular structure.

On the other hand, motivated by the global energy demand in this century, rechargeable lithium-ion batteries (LIBs) have resulted[33−38] in a surge of interest as the state-of-the-art power sources for electronic devices, such as mobile phones and laptops, as well as electric cars because of their high energy and power densities. A wide variety of redox-active organic materials such as small molecules,[15,39] polymers,[12,40,41] and salts[42,43] have been investigated as active materials in rechargeable LIBs over the past few decades.[44] In addition to its remarkable redox-active characteristics and high thermal stability, (−)-**3NDI-Δ** is only sparingly soluble in non-aqueous electrolyte solvents. We therefore employed it recently[45] as the active material in organic rechargeable LIBs. Remarkably, the (−)-**3NDI-Δ**-based organic batteries accessed 95% of their theoretical capacity (154.8 mAh g^{-1}) at a current rate of 0.1C, while also being able to operate with a capacity of 58.1 mAh g^{-1} at ultrahigh rates (100C). Furthermore, a capacity of 71.1 mAh g^{-1} is maintained at 10C, even after cycling for 300 cycles. Control experiments carried out on the monomeric reference compound **Ref-NDI** led to poor rate capabilities and cycling performance, attributed[45] primarily to the higher solubility of **Ref-NDI** in the battery electrolytes. Despite the fact that a three-dimensional rigid nanoporous framework of the organic active material plays a role[46,47] in achieving high cell performances, a comprehensive understanding of structure−performance relationships has still to be explored. It remains, therefore, a puzzle

DOI: 10.1021/jacs.6b02086
J. Am. Chem. Soc. 2016, 138, 5968−5977

as to what happens to the properties of molecular triangles if one replaces the three identical NDI subunits in stepwise fashion with, for instance, PMDI subunits, having almost identical dimensions to those of NDI subunits, and without disrupting the shape-persistent triangular framework. The rational design of this series of diimide-based isosceles triangles is of particular interest in this present investigation.

In the quest to advance our understanding of how the molecular composition of two classes of non-identical redox-active PMDI and NDI units within the isosceles triangles affects the properties associated with (i) through-space electron sharing, (ii) their cooperative solid-state packing, and (iii) the remarkable electrochemical cell performance, we have designed and synthesized (Figure 1) two chiral isosceles triangles—namely, (−)-**1PMDI-2NDI-Δ** and (−)-**2PMDI-1NDI-Δ**. We have also characterized and analyzed the spectroscopic, magnetic, and electrochemical properties of (−)-**1PMDI-2NDI-Δ** and (−)-**2PMDI-1NDI-Δ** and compared our results with those of the previously reported chiral equilateral triangles—namely, (−)-**3NDI-Δ**[29] and (−)-**3PMDI-Δ**[48]—as well as the related (Figure 1c) monomeric reference compounds, **Ref-NDI**[49] and **Ref-PMDI**.[50] Finally, the structure−performance relationships of batteries fabricated using this series of diimide-based molecular triangles were investigated.

RESULTS AND DISCUSSION

The two chiral isosceles triangles were prepared by stepwise condensations between commercially available (*RR*)-*trans*-1,2-cyclohexanediamine and two different dianhydride derivatives—namely, naphthalenetetracarboxylic dianhydride (NDA) and pyromellitic dianhydride (PMDA). The condensation between (*RR*)-*trans*-1,2-cyclohexanediamine and a 5-fold excess of either NDA or PMDA in either DMF or acetic acid gave (Figure 1a,b) the corresponding dimers—namely, (−)-**2NIA**[2] and (−)-**2PMIA**, respectively, in 60−65% yield. The condensation of 2 equiv of (*RR*)-*trans*-1,2-cyclohexanediamine with 1 equiv of either NDA or PMDA in the presence of 2 equiv of *p*-TsOH in DMF or acetic acid gave the corresponding ditosylates of (−)-**1NDI-2NH$_2$** and (−)-**1PMDI-2NH$_2$**, respectively. The subsequent extraction of these salts with a saturated aqueous $NaHCO_3$ solution afforded (Figure 1a,b) the diamines (−)-**1NDI-2NH$_2$** and (−)-**1PMDI-2NH$_2$** in 60−65% yield. Macrocyclizations carried out in DMF at 130 °C by the cyclocondensation of 1 equiv of (−)-**2NIA** with 1 equiv of (−)-**1PMDI-2NH$_2$** afforded the desired isosceles triangle (−)-**1PMDI-2NDI-Δ** in 50% yield, while the cyclocondensation of 1 equiv of (−)-**2PMIA** with 1 equiv of (−)-**1NDI-2NH$_2$** afforded (Figure 1a,b, see the Supporting Information for more details) the desired isosceles triangle (−)-**2PMDI-1NDI-Δ** in 50% yield. Characterization of both (−)-**1PMDI-2NDI-Δ** and (−)-**2PMDI-1NDI-Δ** was achieved by electrospray ionization high-resolution mass spectrometry (ESI-HRMS), which confirmed the presence of the species $[M + H]^+$ in the gas phase at m/z = 989.2779 and 939.2607, respectively.

NMR Spectroscopy. ^{1}H NMR spectra (Figure 2 and Figures S1−S8) of (−)-**1PMDI-2NDI-Δ** and (−)-**2PMDI-1NDI-Δ** recorded in $CDCl_3$ display characteristic resonances for the protons of both the NDI and PMDI subunits in the downfield regions with δ = 8.2−9.0 and 7.8−8.2 ppm, respectively, as well as the aliphatic methine (−CH) and methylene ($-CH_2$) protons of the cyclohexane linkers in the upfield regions with δ = 3.0−6.5 and 1.5−3.0 ppm, respectively. In particular, ^{1}H NMR spectrum of (−)-**1PMDI-2NDI-Δ** shows (Figure 2b) four sets of signals for the eight NDI protons and only one singlet for the two PMDI protons, while that of (−)-**2PMDI-1NDI-Δ** shows (Figure 2c) two sets of signals for the four NDI protons and two doublets for the four PMDI protons. At higher field, three sets of signals were observed for the six methine protons in both (−)-**1PMDI-2NDI-Δ** and (−)-**2PMDI-1NDI-Δ**. A comparison of the ^{1}H NMR spectra (Figure 2), along with ^{13}C NMR spectra (Figure S9), of this series of triangles confirms the lower symmetry (C_2 point group) of the isosceles triangles (−)-**1PMDI-2NDI-Δ** and (−)-**2PMDI-1NDI-Δ** in comparison to the equilateral triangles (−)-**3NDI-Δ** and (−)-**3PMDI-Δ** belonging to the D_3 point group. Furthermore, variable-temperature ^{1}H NMR was performed[51] (Figure 3) on (−)-**2PMDI-1NDI-Δ** to evaluate the rates of rotation of the PMDI and NDI units around the C−N···N−C bond axis of the isosceles triangle. At higher temperatures, coalescence of the two doublets into one broad signal was observed for the PMDI protons (H_C and $H_{C'}$).[52] The free energy of activation at the coalescence temperature (426 K) was calculated[53] to be 23 kcal mol^{-1}.

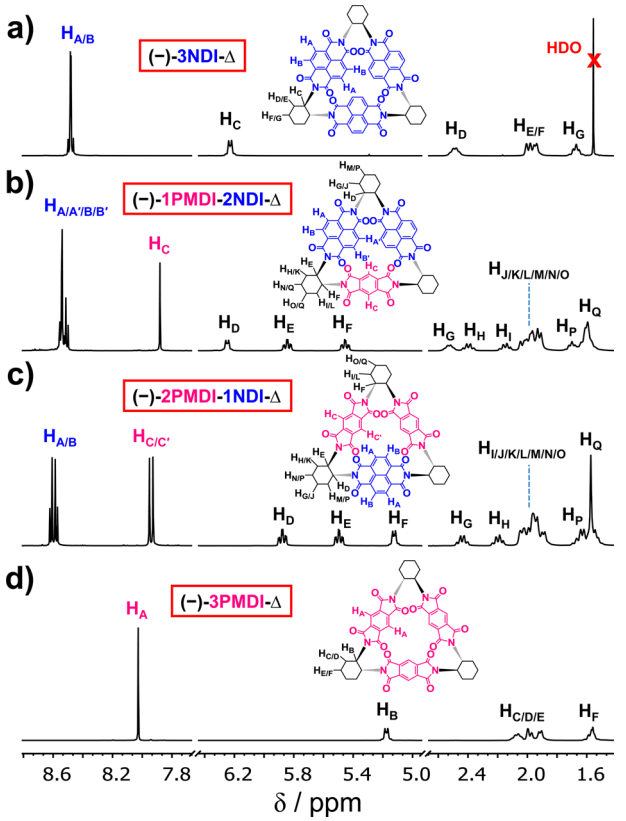

Figure 2. Comparison of the annotated ^{1}H NMR spectra (500 MHz, $CDCl_3$, 298 K) of the molecular triangles (a) (−)-**3NDI-Δ**, (b) (−)-**1PMDI-2NDI-Δ**, (c) (−)-**2PMDI-1NDI-Δ**, and (d) (−)-**3PMDI-Δ**. The signals corresponding to the aromatic protons of the NDI and PMDI subunits, and the aliphatic protons of the cyclohexano linkers, are annotated in blue, magenta, and black, respectively. The unambiguous assignment of the axial and equatorial protons of the cyclohexano linkers is presented in the Supporting Information.

Single-Crystal X-ray Diffraction (XRD) Analyses. In order to gain more insight into the structural details of these isosceles triangles, we performed single-crystal XRD analyses

DOI: 10.1021/jacs.6b02086
J. Am. Chem. Soc. 2016, 138, 5968−5977

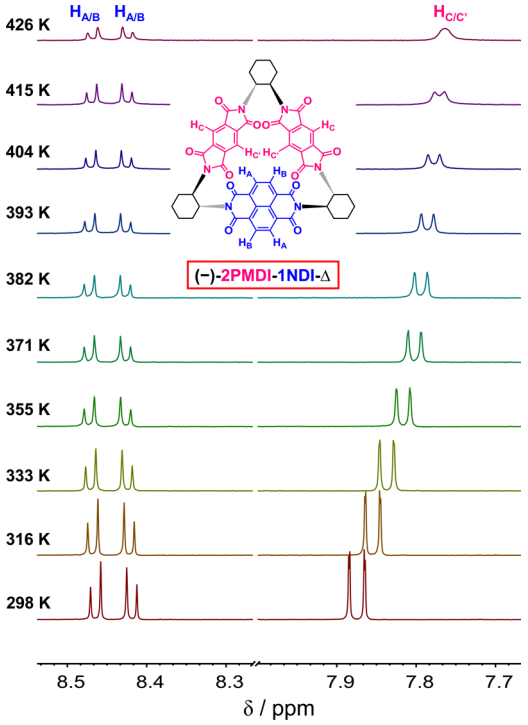

Figure 3. Variable-temperature ^{1}H NMR spectra (600 MHz, CD_3SOCD_3) in the aromatic region of the isosceles triangle (−)-**2PMDI-1NDI-Δ**. The coalescence temperature of the resonances for the PMDI protons (H_C and $H_{C'}$) is observed to be 426 K.

(Figures 4 and 5) on the crystals obtained (i) by slow vapor diffusion of *n*-hexane into a 3.0 mM solution of (−)-**1PMDI-2NDI-Δ** in 1,2-dibromoethane (DBE) and (ii) by slow vapor

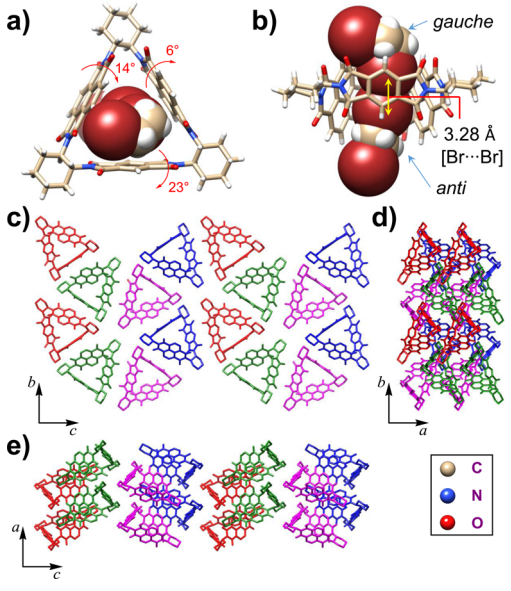

Figure 4. Solid-state (super)structures of (−)-**1PMDI-2NDI-Δ**. (a,b) Plan and side-on views of the inclusion complex formed between (−)-**1PMDI-2NDI-Δ** and two [Br···Br]-bonded 1,2-dibromoethanes, which are depicted in space-filling representations. (c−e) Three views of the packing superstructure of (−)-**1PMDI-2NDI-Δ**, where the 1,2-dibromoethane molecules and H atoms are omitted for the sake of clarity. The four non-equivalent units (−)-**1PMDI-2NDI-Δ** are highlighted in red, green, blue, and magenta, respectively.

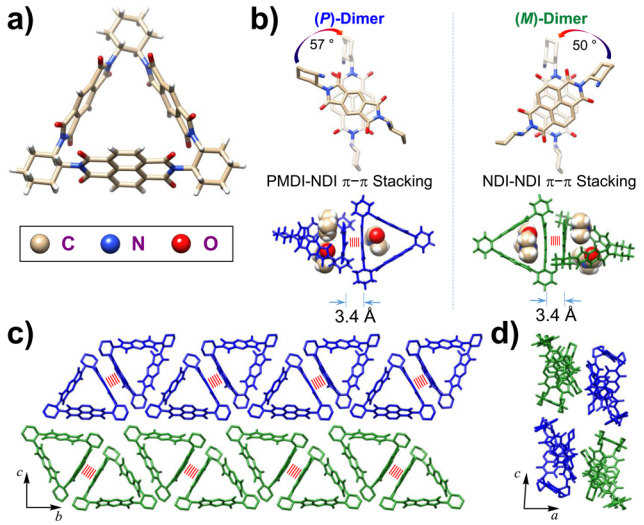

Figure 5. Solid-state (super)structures of (−)-**2PMDI-1NDI-Δ**. (a) Tubular representation of the triangular (−)-**2PMDI-1NDI-Δ**. (b) Top: Two different types of $\pi-\pi$ stacking dimers [(*P*)- and (*M*)-**Dimers**] exhibiting opposite supramolecular helicities; the NDI and PMDI moieties not involved in $\pi-\pi$ stacking are omitted for the sake of clarity. Bottom: The location of DMF molecules inside the triangles and the $\pi-\pi$ stacking of NDI···NDI as well as PMDI···NDI. For the sake of clarity, the (*P*)-**Dimer** is depicted in blue, and the (*M*)-**Dimer** is depicted in green. (c,d) Plan and side-on views of the superstructure of both the (*P*)- and (*M*)-**Dimers**. Red hatched lines indicate the $\pi-\pi$ stacking interactions between the aromatic subunits.

diffusion of H_2O into a 5.0 mM solution of (−)-**2PMDI-1NDI-Δ** in DMF over the course of 3 days. The solid-state (super)structure (Figure 4) of (−)-**1PMDI-2NDI-Δ** reveals the rigid geometries of the triangular hollow prism in which the tilt angles of the PMDI (23°) and the two NDI subunits (6 and 14°) are much greater than those[29,30] of three NDI subunits (∼3°) in the equilateral triangle (−)-**3NDI-Δ**. This observation indicates that the less-bulky PMDI unit facilitates the tilting of all three π-surfaces. In striking contrast to the tubular superstructure of (−)-**3NDI-Δ** in DBE, that of (−)-**1PMDI-2NDI-Δ** in DBE reveals (Figure 4c−e) neither columnar stacking of the triangular units to form one-dimensional (1D) nanotubes nor $\pi-\pi$ stacking between two NDI units or PMDI and NDI units. Although the cavity of (−)-**1PMDI-2NDI-Δ** is penetrated (Figure 4a,b) by two [Br···Br]-bonded (3.28 Å) DBE molecules which are stabilized by [Br···π] interactions (∼3.5 Å) with π-surfaces, only one DBE molecule is in *anti*-conformation, and the other is in the *gauche*-conformation (Figure 4b), which prohibits the formation of continuous 1D [Br···Br]-bonded solvent chains that would template the formation of the nanotubes.[30] The replacement of the NDI subunits with PMDI ones within the triangle also breaks the complementarity of [C−H···O] interactions between two triangles, which is crucial for their columnar stacking.

Although we were unable to obtain suitable single crystals of (−)-**2PMDI-1NDI-Δ** from DBE/*n*-hexane for XRD analysis, the compound did crystallize from the aqueous DMF system. The solid-state structure of (−)-**2PMDI-1NDI-Δ** reveals (Figure 5a) a similar rigid triangular geometry. Among three of the four asymmetric units in the unit cell, one or two DMF molecules are bound (Figure 5b, bottom) to their cavities by means of very short $\pi-\pi$ overlap (∼3.0 Å) between the amide groups of DMF and the NDI planes. Much to our surprise,

DOI: 10.1021/jacs.6b02086
J. Am. Chem. Soc. 2016, 138, 5968−5977

these four isosceles triangles assemble (Figure 5b) into two types of $\pi-\pi$ stacking supramolecular dimers—(i) (*P*)-helical dimer [**(*P*)-Dimer**, Figure 5b, left] with a right-twisted angle of 57° formed through $\pi-\pi$ stacking (3.4 Å) between the DMF-bound NDI plane of one triangle and a PMDI plane of another triangle, and (ii) (*M*)-helical dimer [**(*M*)-Dimer**, Figure 5b, right] with a left-twisted angle of 50° formed through $\pi-\pi$ stacking (3.4 Å) between DMF-bound NDI planes of another two triangles. It is worth noting that, prior to this work, $\pi-\pi$ stacking between NDI units of molecular triangles had been observed only in the cases of host–guest complexes[29] [$I_3^-\subset$**3NDI-Δ**] of **3NDI-Δ** with I_3^- and the radical anion[32] [(−)-**3NDI-Δ**]$^{\bullet-}$ of (−)-**3NDI-Δ** on account of the increase in the electron density of the neutral NDI unit as a result of anion binding and reduction, respectively. In the case of (−)-**2PMDI-1NDI-Δ**, it appears that DMF acts in a role similar to that of I_3^- in increasing the electron density of the NDI unit through very short $\pi-\pi$ stacking which favors the $\pi-\pi$ stacking of another facet of the NDI unit with the other π-plane. The helicity of supramolecular assembles is determined predominantly by the chirality of the chiral monomer.[29,30] In the superstructure of (−)-**2PMDI-1NDI-Δ**, however, the assembly of the homochiral monomers gives rise to two types of dimers with opposite supramolecular helicities. While the (*M*)-**Dimer**, formed through NDI–NDI $\pi-\pi$ stacking, retains (*M*)-helicity which is consistent with that observed[29,32] in the $\pi-\pi$ stacking assemblies of (−)-**3NDI-Δ**, the (*P*)-**Dimer** formed through NDI–PMDI $\pi-\pi$ stacking shows (*P*)-helicity. The plausible mechanism for the coexistence of both these dimers can be explained by the fact that the less-bulky PMDI is unable to restrict the effect of the stereogenic centers of the (*RR*)-*trans*-1,2-cyclohexano groups for specifically forming the corresponding (*M*)-helicity. Both (*P*)- and (*M*)-**Dimers** assemble (Figure 5c) to form 1D tapes along the *b*-axis, respectively, which then pack (Figure 5d) alternatively in the *a*–*c* plane to form the crystals. Strikingly, both X-ray superstructures of (−)-**1PMDI-2NDI-Δ** and (−)-**2PMDI-1NDI-Δ** exhibit a common feature—that is, there is no columnar stacking of either triangle to form 1D nanotubes, an observation which indicates that the breaking of symmetry of the triangles hinders the complementarity of [C–H···O] hydrogen-bonding interactions between the columnar stacked triangles; consequently, these observations highlight the necessity of the symmetry of (−)-**3NDI-Δ** in order to provide complementary [C–H···O] interactions for driving the formation of 1D columnar stacking nanotubes.[30]

UV/Vis Absorption and Circular Dichroism (CD) Spectroscopies. The optical properties of all the triangles were investigated (Figure 6a) by UV/Vis absorption spectroscopy. The comparison of the absorption spectra of this series of triangles suggests that the intensity of the absorption peaks with maxima at 360 and 380 nm decreases gradually on going from (−)-**3NDI-Δ** to (−)-**1PMDI-2NDI-Δ** to (−)-**2PMDI-1NDI-Δ** and eventually disappears in the case of (−)-**3PMDI-Δ**, in line with the decrease in the number of NDI subunits present in the triangle. This observation is consistent with the characteristic 0←0 and 0←1 vibronic bands corresponding to the $S_1\leftarrow S_0$ electronic transition of the NDI subunits. On the other hand, the intensity of the absorption peaks in the region 225–280 nm rises with the increase in the number of PMDI subunits, an observation which is in good agreement with the characteristic *z*-polarized $\pi-\pi^*$ electronic transitions[48] of the PMDI units.

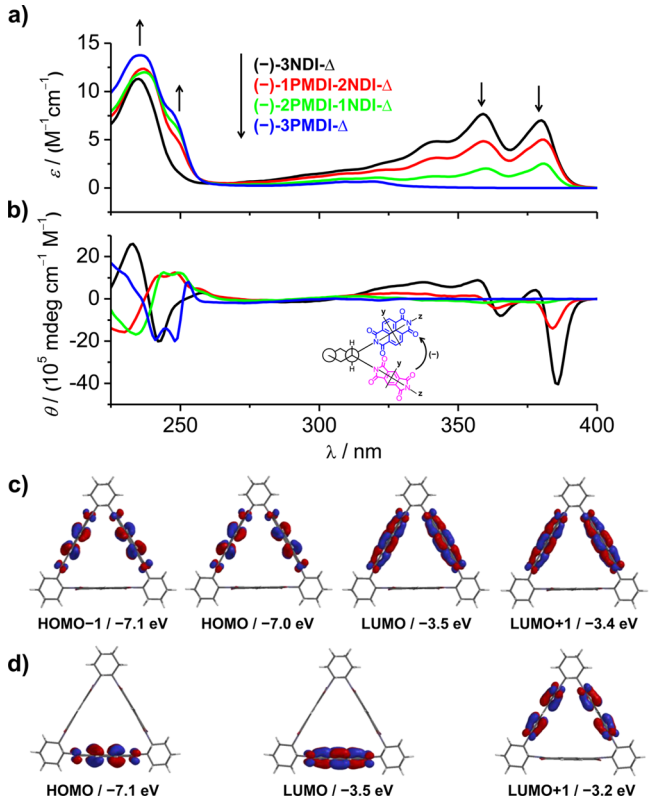

Figure 6. (a) UV/vis absorption and (b) CD spectra of (−)-**3NDI-Δ** (black traces), (−)-**1PMDI-2NDI-Δ** (red traces), (−)-**2PMDI-1NDI-Δ** (green traces), and (−)-**3PMDI-Δ** (blue traces) recorded in CH_2Cl_2 at 298 K. Graphical representations of the DFT-calculated (B3LYP/6-31G*) FMOs of the molecular triangles showing the available (c) HOMO−1, HOMO, LUMO, and LUMO+1 levels of (−)-**1PMDI-2NDI-Δ** and (d) HOMO, LUMO, and LUMO+1 levels of (−)-**2PMDI-1NDI-Δ**. FMO refers to the frontier molecular orbital, HOMO refers to the highest occupied molecular orbital, and LUMO refers to the lowest unoccupied molecular orbital. Orbital isosurfaces are illustrated at 0.004 electron Bohr^{-3}.

CD spectroscopy (Figure 6b) was also performed in order to probe the chiroptical properties and Cotton effects generated by the inter-chromophoric exciton coupling of the neighboring NDI or PMDI subunits within a given triangle. Characteristically strong negative exciton Cotton effects are observed (Figure 6b) in the range 350–400 nm, originating from the coupling of the $\pi-\pi^*$ electronic transitions polarized along the long *z*-axis of the NDI subunits (Band I region) in the case of the triangles (−)-**3NDI-Δ** and (−)-**1PMDI-2NDI-Δ**, while these strong negative exciton Cotton effects in this region are not observed in the case of the triangles (−)-**2PMDI-1NDI-Δ** and (−)-**3PMDI-Δ**, because of the absence of more than one neighboring NDI unit to promote the exciton coupling.[54] It should be noted that the negative Cotton effects observed here are consistent with the absolute (*RRRRRR*)-configuration of the triangles. In the case of (−)-**3NDI-Δ**, the strong negative Cotton effect observed (Figure 6b) at 242 nm originates from the coupling of the $\pi-\pi^*$ transitions polarized along the short *y*-axis of the NDI subunits (Band II region). On the other hand, the strong negative exciton couplet at 240 and 248 nm in the case of (−)-**3PMDI-Δ** appears as a consequence of the coupling of the $\pi-\pi^*$ transitions polarized along both the long *z*-axis and the short *y*-axis of the PMDI subunits, respectively. In the case of the isosceles triangles (−)-**1PMDI-2NDI-Δ** and

DOI: 10.1021/jacs.6b02086
J. Am. Chem. Soc. 2016, 138, 5968–5977

(−)-**2PMDI-1NDI-Δ**, the negative exciton Cotton effects observed in the region 225−240 nm are presumably influenced by the multiple exciton couplings of the transition dipoles polarized along both the long *z*- and the short *y*-axes of the PMDI and the short *y*-axis of the NDI subunits.

Cyclic Voltammetry (CV). We first performed CV experiments (Figure 7) in CH_2Cl_2 on the two isosceles

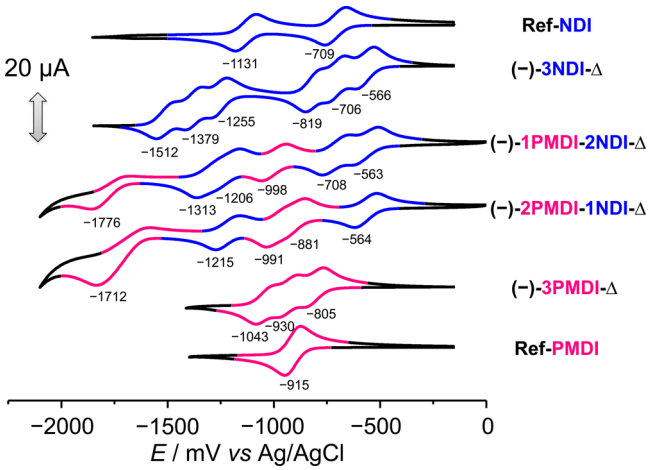

Figure 7. Solution-state CVs (0.5 mM in CH_2Cl_2, 100 mM $TBAPF_6$, 50 mV s^{-1}, 298 K) of **Ref-NDI**, (−)-**3NDI-Δ**, (−)-**1PMDI-2NDI-Δ**, (−)-**2PMDI-1NDI-Δ**, (−)-**3PMDI-Δ**, and **Ref-PMDI**. Half-wave peak potentials ($E_{1/2}$) are shown in mV.

triangles [(−)-**1PMDI-2NDI-Δ** and (−)-**2PMDI-1NDI-Δ**] and compared these results with those of the equilateral triangles [(−)-**3NDI-Δ** and (−)-**3PMDI-Δ**] as well as with the monomeric reference compounds (**Ref-NDI** and **Ref-PMDI**). While the CV of the **Ref-NDI** shows two distinct reversible one-electron waves with half-wave potentials at −709 and −1131 mV vs Ag/AgCl, corresponding to the formation of the $[\mathbf{Ref\text{-}NDI}]^{\bullet-}$ radical anion and the $[\mathbf{Ref\text{-}NDI}]^{2-}$ dianion, respectively, the CV of (−)-**3NDI-Δ** shows clear splittings into six distinct reversible one-electron redox processes. Similarly, the CV of the **Ref-PMDI** shows a reversible one-electron reduction process at −915 mV, corresponding to the formation of the $[\mathbf{Ref\text{-}PMDI}]^{\bullet-}$ radical anion, while the CV of (−)-**3PMDI-Δ** also shows clear splittings into three distinct reversible one-electron waves.[55] Strikingly, the CV of (−)-**1PMDI-2NDI-Δ** displays (Figure 7) multiple reduction processes involving a total of six electrons—namely, (i) two sequential distinct reversible one-electron waves at −563 and −708 mV, corresponding to the formation of two singly reduced $[\mathbf{NDI}]^{\bullet-}$ radical anions, (ii) a reversible one-electron wave at −998 mV, corresponding to the formation of a singly reduced $[\mathbf{PMDI}]^{\bullet-}$ radical anion, (iii) two closely following reversible one-electron processes at −1206 and −1313 mV, corresponding to the formation of two doubly reduced $[\mathbf{NDI}]^{2-}$ dianions, and (iv) finally, a quasi-reversible one-electron process at −1776 mV, corresponding to the formation of a doubly reduced $[\mathbf{PMDI}]^{2-}$ dianion. Also, the CV of (−)-**2PMDI-1NDI-Δ** displayed (Figure 7) multiple features containing six electrons in total—namely, (i) a reversible one-electron reduction process at −564 mV, corresponding to the formation of a singly reduced $[\mathbf{NDI}]^{\bullet-}$ radical anion, (ii) two closely following reversible one-electron reduction waves at −881 and −991 mV, corresponding to the formation of two singly reduced $[\mathbf{PMDI}]^{\bullet-}$ radical anions, (iii) a reversible one-electron reduction wave at −1215 mV, corresponding to the formation of a singly reduced $[\mathbf{NDI}]^{2-}$ dianion, and (iv) finally, a quasi-reversible two-electron process at −1712 mV, corresponding to the formation of two doubly reduced $[\mathbf{PMDI}]^{2-}$ dianions. Although the first reduction potential ($E_1 \approx -564$ mV) of the NDI unit in all of the NDI-containing triangles [(−)-**3NDI-Δ**, (−)-**1PMDI-2NDI-Δ**, (−)-**2PMDI-1NDI-Δ**] is nearly constant and shifted by 145 mV toward more positive potentials compared with that of **Ref-NDI** (E_1 = −709 mV), the subsequent reduction potentials can be tuned significantly, thus establishing a set of unique molecular triangles for structure−property relationship investigations and the device fabrication of efficient energy storage. All of these observations suggest that, despite having two types of non-identical neighboring redox-active units within triangular architectures, each molecular triangle can accept reversibly up to six electrons.

EPR/ENDOR Spectroscopy. In order to gain more insight into the through-space electron sharing among the neighboring redox-active NDI and PMDI units within the molecular triangles, continuous-wave electron paramagnetic resonance (CW-EPR) and electron−nuclear double-resonance (ENDOR) spectroscopies were carried out on the monoreduced radical anions of the triangles generated by adding 1 equiv of cobaltocene ($CoCp_2$) as the chemical reductant. Solution-phase CW-EPR spectra of $[(-)\text{-}\mathbf{3NDI\text{-}\Delta}]^{\bullet-}$ and $[(-)\text{-}\mathbf{1PMDI\text{-}2NDI\text{-}\Delta}]^{\bullet-}$ monoradical anions reveal (Figure 8a) a decrease in the spectral width which corresponds to a decrease in the magnitude of the nuclear hyperfine interactions, relative to that of $[\mathbf{Ref\text{-}NDI}]^{\bullet-}$. In contrast, the EPR spectrum of $[(-)\text{-}\mathbf{2PMDI\text{-}1NDI\text{-}\Delta}]^{\bullet-}$ matches nearly perfectly with that

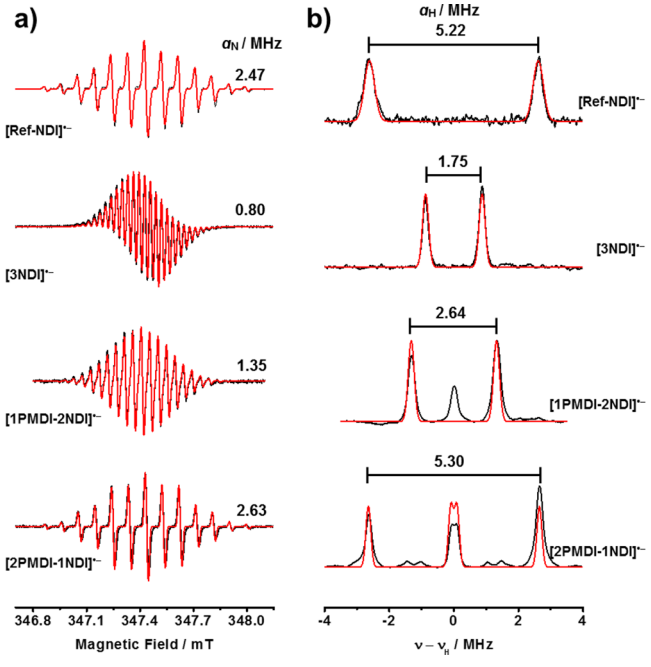

Figure 8. (a) CW-EPR and (b) ^{1}H ENDOR spectra (0.25 mM in CH_2Cl_2, 298 K) of $[\mathbf{Ref\text{-}NDI}]^{\bullet-}$, $[(-)\text{-}\mathbf{3NDI\text{-}\Delta}]^{\bullet-}$, $[(-)\text{-}\mathbf{1PMDI\text{-}2NDI\text{-}\Delta}]^{\bullet-}$, and $[(-)\text{-}\mathbf{2PMDI\text{-}1NDI\text{-}\Delta}]^{\bullet-}$, formed by the mono-reduction of their corresponding neutral states by adding 1 equiv of cobaltocene. Overlay between the experimental spectra (black traces) and their simulated spectra (red traces). Isotropic nitrogen and proton hyperfine coupling constants were obtained from simulation of the CW-EPR and ^{1}H ENDOR, respectively.

DOI: 10.1021/jacs.6b02086
J. Am. Chem. Soc. 2016, 138, 5968−5977

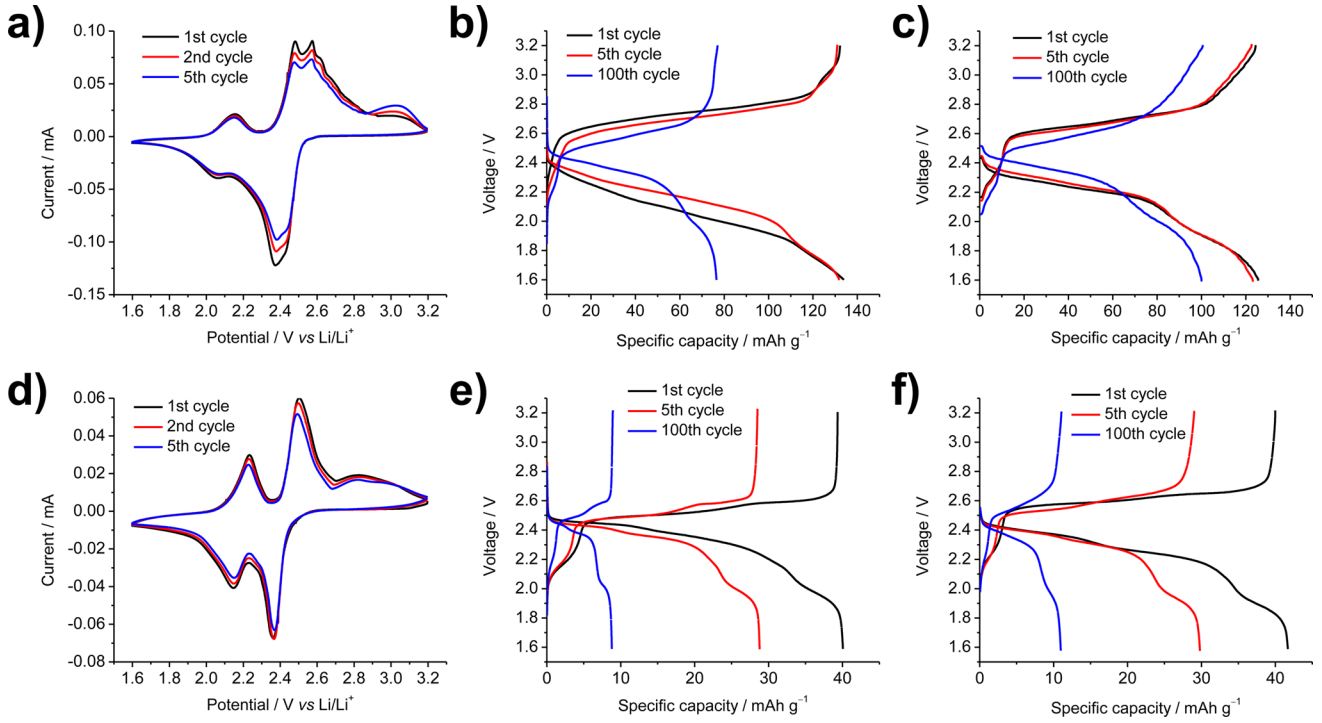

Figure 9. Solid-state CVs and charge/discharge properties of the (−)-**1PMDI-2NDI-Δ** and (−)-**2PMDI-1NDI-Δ** batteries. CV profiles of the first, second, and fifth cycles recorded at a scan rate of 0.05 mV s^{-1} for the (a) (−)-**1PMDI-2NDI-Δ** battery and (d) (−)-**2PMDI-1NDI-Δ** battery. Charge/discharge profiles for the first, fifth, and hundredth cycles at rates of (b) 0.5C and (c) 1.0C for the (−)-**1PMDI-2NDI-Δ** battery. Charge/discharge profiles for the first, fifth, and hundredth cycles at rates of (e) 0.5C and (f) 1.0C for the (−)-**2PMDI-1NDI-Δ** battery.

of [**Ref-NDI**]$^{\bullet-}$; i.e., no significant change in spectral width or number of lines is observed. The CW-ENDOR spectra of [(−)-**3NDI-Δ**]$^{\bullet-}$ and [(−)-**1PMDI-2NDI-Δ**]$^{\bullet-}$ reveal (Figure 8b) an obvious decrease in the isotropic hyperfine coupling constants (a_H) by factors of ca. 3 and 2, respectively, relative to those of [(−)-**2PMDI-1NDI-Δ**]$^{\bullet-}$ and [**Ref-NDI**]$^{\bullet-}$.[56] According to the McConnell relation, the hydrogen isotropic hyperfine coupling constant is proportional to the unpaired spin density at the adjacent carbon[56] and should therefore decrease linearly with the number of NDI subunits which share the unpaired spin density. The observed decrease in the hydrogen isotropic hyperfine coupling constants suggests that the unpaired spin density is shared among all of the NDI subunits present within a given molecular triangle on the time scale (10^7 s^{-1}) of the electron−nuclear hyperfine interaction. Moreover, simulation of the CW-EPR spectra confirmed that only the NDI subunits present within the molecular triangles contribute to the spectrum.

Density Functional Theory (DFT) Calculations. Previously, we performed[29] DFT calculations on the equilateral triangles: they revealed the presence of delocalized frontier molecular orbitals (FMOs) located on all of the three symmetrically equivalent NDI subunits in the LUMO of (−)-**3NDI-Δ**, supporting the CV and EPR results commensurate with cyclic through-space electron sharing among all the neighboring NDI subunits. We therefore performed (Figure 6c,d) similar DFT calculations using a continuum solvent model with the functional B3LYP/6-31G* on the two isosceles triangles (−)-**1PMDI-2NDI-Δ** and (−)-**2PMDI-1NDI-Δ** to confirm where the delocalized FMOs are located in each case. We observed (Figure 6c,d) that the LUMO, as well as LUMO +1, of (−)-**1PMDI-2NDI-Δ** are located only on the two NDI subunits present, while the LUMO of (−)-**2PMDI-1NDI-Δ** is located only on the one available NDI subunit. These calculations are consistent with the CV, as well as EPR/ENDOR results, supporting the through-space sharing of the unpaired electron selectively by the NDI subunits present in the case of the monoreduced radical anions [(−)-**1PMDI-2NDI-Δ**]$^{\bullet-}$ and [(−)-**2PMDI-1NDI-Δ**]$^{\bullet-}$. The LUMO+1 of (−)-**2PMDI-1NDI-Δ** is located, however, on both of the PMDI subunits present in the triangle, indicating that the two subsequent reductions of the monoradical anion to di- and triradical anionic states occur on the two electronically communicating PMDI subunits.

Solid-State Cyclic Voltammetry. Motivated by our earlier research[45] on the remarkable cell performance given by the equilateral triangle (−)-**3NDI-Δ** as an active material in organic rechargeable LIBs, we decided to investigate the structure−performance relationship of this unique set of molecular triangles, namely (−)-**3NDI-Δ**, (−)-**1PMDI-2NDI-Δ**, and (−)-**2PMDI-1NDI-Δ**. The electrochemical performance of these triangles was characterized using CR2032-type coin cells. The electrodes were prepared by mixing 50 wt% active material [(−)-**1PMDI-2NDI-Δ** or (−)-**2PMDI-1NDI-Δ**], 40 wt% carbon black, and 10 wt% polyvinylidene fluoride (PVDF) binder in anhydrous *N*-methyl-2-pyrrolidone (NMP) to form a well-dispersed slurry, followed by coating on aluminum foil and drying under vacuum at 120 °C for 24 h.

The solid-state CV of (−)-**1PMDI-2NDI-Δ** displayed (Figure 9a) three sets of peaks, centered at 2.50, 2.43, and 2.10 V vs Li/Li^+, presumably corresponding to (i) the two-electron (monoreduction of two NDI subunits to two [**NDI**]$^{\bullet-}$ radical anions), (ii) the three-electron (first reduction of PMDI subunit to [**PMDI**]$^{\bullet-}$ radical anion and subsequent reduction of two [**NDI**]$^{\bullet-}$ radical anions to [**NDI**]$^{2-}$ dianions), and (iii) the one-electron (subsequent reduction of [**PMDI**]$^{\bullet-}$ radical

DOI: 10.1021/jacs.6b02086
J. Am. Chem. Soc. 2016, 138, 5968−5977

anion to $[\mathbf{PMDI}]^{2-}$ dianion) redox processes, respectively. Also, the solid-state CV of (−)-**2PMDI-1NDI-Δ** displayed (Figure 9d) only two sets of peaks, centered at 2.43 and 2.19 V vs Li/Li^+, presumably corresponding to the four-electron (double reduction of NDI subunits to $[\mathbf{NDI}]^{2-}$ dianions and the monoreduction of the two PMDI subunits to two $[\mathbf{PMDI}]^{\bullet-}$ radical anions) and two-electron (subsequent reduction of two $[\mathbf{PMDI}]^{\bullet-}$ radical anion subunits to two $[\mathbf{PMDI}]^{2-}$ dianions) redox processes. In addition, the comparison of the solid-state CV (Figure 9a,d) with the solution-state CV (Figure 7) of (−)-**1PMDI-2NDI-Δ** and (−)-**2PMDI-1NDI-Δ** reveals significant overlapping of the peaks in the solid state. This overlap leads to a decrease in the total number of peaks observed, and some of these peaks are not well-resolved. It is interesting to note (Figure 9a,d) that the areas of the oxidation and reduction peaks as well as the peak potentials in the solid-state CV remained almost unchanged, with a slight decrease in the current, during cycling for both (−)-**1PMDI-2NDI-Δ** and (−)-**2PMDI-1NDI-Δ**, suggesting that all the redox reactions are highly reversible, even in the solid state. In line with the CV results obtained previously[45] for (−)-**3NDI-Δ**, the good electrochemical stability and reversibility of (−)-**1PMDI-2NDI-Δ** and (−)-**2PMDI-1NDI-Δ** obtained here prompted us to evaluate the structure−performance relationship of these triangles as active materials in organic rechargeable LIBs.

Electrochemical Cell Performance. We investigated[57] the galvanostatic measurements of the batteries at different current rates of 0.5 and 1.0C.[58] In the case of (−)-**1PMDI-2NDI-Δ**, a three-step charge/discharge profile was noted upon careful observation at rates of 0.5 and 1.0C (Figure 9b,c). The not so well-defined plateaus displayed in the charge/discharge profile of the (−)-**1PMDI-2NDI-Δ** battery at about 2.3 and 2.0 V match the CV results (Figure 9a). The experimental charge and discharge capacities (Figure 9b) of the (−)-**1PMDI-2NDI-Δ** battery at 0.5C are 132.2 and 133.9 mAh g^{-1}, corresponding to 81 and 82% of the theoretical capacity (162.6 mAh g^{-1}) of (−)-**1PMDI-2NDI-Δ**, respectively. The cycling performance of the (−)-**1PMDI-2NDI-Δ** battery was also tested (Figure S10) at current rates of 0.5 and 1.0C. While a slight discharge capacity decay was observed during the initial cycling, the rate of decay is improved when the current rate is increased from 0.5 to 1.0C (Figure 9 and Figure S10).

Similar experiments performed on the (−)-**2PMDI-1NDI-Δ** battery also revealed (Figure 9e,f) a more well-defined charge/discharge profile upon careful observation at rates of 0.5 and 1.0C. Surprisingly, the experimental charge and discharge capacities of (−)-**2PMDI-1NDI-Δ** battery at 0.5C are 39.4 and 40.1 mAh g^{-1}, corresponding to only 23.0 and 23.5% of the theoretical capacity (171.3 mAh g^{-1}) of (−)-**2PMDI-1NDI-Δ**. By contrast, the cycling performance of the (−)-**2PMDI-1NDI-Δ** battery showed (Figure S10) a rapid decay of the capacity. The poor performance observed for the (−)-**2PMDI-1NDI-Δ** battery, compared with that of the (−)-**1PMDI-2NDI-Δ** battery, could be attributed to the increased solubility[59,60] of the neutral as well as the reduced states of the (−)-**2PMDI-1NDI-Δ**-based active material under the galvanostatic measurement conditions.

Overall, the comparisons of the rate performance and cycling stability of this series of diimide-based batteries containing (−)-**3NDI-Δ**, (−)-**1PMDI-2NDI-Δ**, and (−)-**2PMDI-1NDI-Δ** suggest that the electrochemical cell performance of the batteries follows[45,61] the order (−)-**3NDI-Δ** > (−)-**1PMDI-2NDI-Δ** > (−)-**2PMDI-1NDI-Δ**. From these data, it can be concluded that the replacement of the NDI with PMDI subunits within the molecular triangle can dramatically increase the solubility of the resultant active material in the battery electrolytes. These observations are in good agreement with the literature report[14] which suggests that the PMDI derivatives are noted to deliver lower capacities compared with their NDI counterparts, on account of the larger electron affinity of the NDI units.

CONCLUSIONS

In summary, two chiral isosceles triangles (−)-**1PMDI-2NDI-Δ** and (−)-**2PMDI-1NDI-Δ** have been synthesized. Comparison of the ^1H NMR spectra of these two triangles with those of the previously characterized[29,48] equilateral triangles [(−)-**3NDI-Δ** and (−)-**3PMDI-Δ**] is consistent with the lower symmetries (C_2 point groups) of these two isosceles triangles. The solid-state (super)structures of the isosceles triangles, grown from both 1,2-dibromoethane/*n*-hexane and DMF/H_2O, reveal the formation of 2D layer-like superstructures, confirming the lack of ability of the isosceles triangles to form extended 1D tubular superstructures as previously observed[30] in the case of (−)-**3NDI-Δ**. Specifically, (−)-**2PMDI-1NDI-Δ**, in the presence of DMF, forms two different types of intermolecular NDI−NDI and NDI−PMDI $\pi-\pi$ stacking dimers [(***P***)- and (***M***)-**Dimers**] with opposite supramolecular helicities. CV suggests that through-space electronic communication between the identical NDI−NDI or PMDI−PMDI units in the isosceles triangles produces up to six accessible redox states. It should be noted that both the EPR and ENDOR experiments, supported by DFT calculations, in the case of monoreduced radical anions of the isosceles triangles indicate that the unpaired electron is shared selectively among the adjacent NDI—but not PMDI—units within the triangular geometries. The isosceles triangles, when employed as active materials in organic rechargeable lithium-ion batteries, were shown to have capacities of 133.9 and 40.1 mAh g^{-1} for (−)-**1PMDI-2NDI-Δ** and (−)-**2PMDI-1NDI-Δ**, respectively. When compared with the remarkable cell performance we have observed[45] for (−)-**3NDI-Δ**, a good rate performance and cycling stability were noted for (−)-**1PMDI-2NDI-Δ**, while a relatively poor electrochemical performance was recorded for (−)-**2PMDI-1NDI-Δ**, mainly on account of the good solubility of the active material (−)-**2PMDI-1NDI-Δ** in the battery electrolytes. The structure−performance relationships for this series of molecular triangles reveal that the electrochemical cell performance improves as the number of NDI subunits is increased within the triangles. Probing these relationships is providing us with increased understanding on how the rational design of redox-active organic molecules affects their electron transport properties, thus paving the way for the fabrication of next-generation organic electronics and energy storage devices.

ASSOCIATED CONTENT

Supporting Information

The Supporting Information is available free of charge on the ACS Publications website at DOI: 10.1021/jacs.6b02086.

Materials and methods, synthetic protocols, NMR spectra, crystallographic characterization, and cycling performance studies of the batteries, including Figures S1−S10 (PDF)

DOI: 10.1021/jacs.6b02086
J. Am. Chem. Soc. 2016, 138, 5968−5977

X-ray crystallographic file for (−)-**1PMDI-2NDI-Δ** (CIF)

X-ray crystallographic file for (−)-**2PMDI-1NDI-Δ** (CIF)

AUTHOR INFORMATION

Corresponding Author

*stoddart@northwestern.edu

Notes

The authors declare no competing financial interest.

ACKNOWLEDGMENTS

This research is Project No. 34-948 of the Joint Center of Excellence in Integrated Nano-Systems (JCIN) at King Abdulaziz City of Science and Technology (KACST) and Northwestern University (NU). This work was supported by the Chemical Sciences, Geosciences, and Biosciences Division, Office of Basic Energy Sciences, U.S. Department of Energy under grant no. DE-FG02-99ER14999 (M.R.W.). The authors thank both KACST and NU for their continued support of this research. Y.W. thanks the Fulbright Scholar Program for a fellowship and the NU International Institute of Nanotechnology (IIN) for a Ryan Fellowship.

REFERENCES

(1) Susumu, K.; Frail, P. R.; Angiolillo, P. J.; Therien, M. J. *J. Am. Chem. Soc.* **2006**, *128*, 8380.

(2) Wu, Y.; Nalluri, S. K. M.; Young, R. M.; Krzyaniak, M. D.; Margulies, E. A.; Stoddart, J. F.; Wasielewski, M. R. *Angew. Chem., Int. Ed.* **2015**, *54*, 11971.

(3) Sun, D.; Rosokha, S. V.; Kochi, J. K. *Angew. Chem., Int. Ed.* **2005**, *44*, 5133.

(4) Rosokha, S. V.; Neretin, I. S.; Sun, D.; Kochi, J. K. *J. Am. Chem. Soc.* **2006**, *128*, 9394.

(5) Guo, X.; Facchetti, A.; Marks, T. J. *Chem. Rev.* **2014**, *114*, 8943.

(6) Wang, C.; Dong, H.; Hu, W.; Liu, Y.; Zhu, D. *Chem. Rev.* **2012**, *112*, 2208.

(7) Brédas, J.-L.; Calbert, J. P.; da Silva Filho, D.; Cornil, J. *Proc. Natl. Acad. Sci. U. S. A.* **2002**, *99*, 5804.

(8) Katz, H. E.; Lovinger, A. J.; Johnson, J.; Kloc, C.; Siegrist, T.; Li, W.; Lin, Y. Y.; Dodabalapur, A. *Nature* **2000**, *404*, 478.

(9) He, T.; Stolte, M.; Würthner, F. *Adv. Mater.* **2013**, *25*, 6951.

(10) Zheng, Q.; Huang, J.; Sarjeant, A.; Katz, H. E. *J. Am. Chem. Soc.* **2008**, *130*, 14410.

(11) Huang, H.; Zhou, N.; Ortiz, R. P.; Chen, Z.; Loser, S.; Zhang, S.; Guo, X.; Casado, J.; López Navarrete, J. T.; Yu, X.; Facchetti, A.; Marks, T. J. *Adv. Funct. Mater.* **2014**, *24*, 2782.

(12) Han, X.; Chang, C.; Yuan, L.; Sun, T.; Sun, J. *Adv. Mater.* **2007**, *19*, 1616.

(13) Wang, H.-g.; Yuan, S.; Ma, D.-l.; Huang, X.-l.; Meng, F.-l.; Zhang, X.-b. *Adv. Energy Mater.* **2014**, *4*, 1301651.

(14) Song, Z.; Zhan, H.; Zhou, Y. *Angew. Chem., Int. Ed.* **2010**, *49*, 8444.

(15) Häupler, B.; Wild, A.; Schubert, U. S. *Adv. Energy Mater.* **2015**, *5*, 1402034.

(16) Bhosale, S. V.; Jani, C. H.; Langford, S. J. *Chem. Soc. Rev.* **2008**, *37*, 331.

(17) Suraru, S.-L.; Würthner, F. *Angew. Chem., Int. Ed.* **2014**, *53*, 7428.

(18) Sakai, N.; Bhosale, R.; Emery, D.; Mareda, J.; Matile, S. *J. Am. Chem. Soc.* **2010**, *132*, 6923.

(19) Zhan, X.; Facchetti, A.; Barlow, S.; Marks, T. J.; Ratner, M. A.; Wasielewski, M. R.; Marder, S. R. *Adv. Mater.* **2011**, *23*, 268.

(20) Míšek, J.; Vargas Jentzsch, A.; Sakurai, S.-i.; Emery, D.; Mareda, J.; Matile, S. *Angew. Chem., Int. Ed.* **2010**, *49*, 7680.

(21) Santos-Figueroa, L. E.; Moragues, M. E.; Climent, E.; Agostini, A.; Martinez-Manez, R.; Sancenon, F. *Chem. Soc. Rev.* **2013**, *42*, 3489.

(22) Dawson, R. E.; Hennig, A.; Weimann, D. P.; Emery, D.; Ravikumar, V.; Montenegro, J.; Takeuchi, T.; Gabutti, S.; Mayor, M.; Mareda, J.; Schalley, C. A.; Matile, S. *Nat. Chem.* **2010**, *2*, 533.

(23) Vargas Jentzsch, A.; Hennig, A.; Mareda, J.; Matile, S. *Acc. Chem. Res.* **2013**, *46*, 2791.

(24) Zhao, Y.; Domoto, Y.; Orentas, E.; Beuchat, C.; Emery, D.; Mareda, J.; Sakai, N.; Matile, S. *Angew. Chem., Int. Ed.* **2013**, *52*, 9940.

(25) Zhao, Y.; Sakai, N.; Matile, S. *Nat. Commun.* **2014**, *5*, 3911.

(26) Nalluri, S. K. M.; Berdugo, C.; Javid, N.; Frederix, P. W. J. M.; Ulijn, R. V. *Angew. Chem., Int. Ed.* **2014**, *53*, 5882.

(27) Berdugo, C.; Nalluri, S. K. M.; Javid, N.; Escuder, B.; Miravet, J. F.; Ulijn, R. V. *ACS Appl. Mater. Interfaces* **2015**, *7*, 25946.

(28) Mas-Torrent, M.; Rovira, C. *Chem. Rev.* **2011**, *111*, 4833.

(29) Schneebeli, S. T.; Frasconi, M.; Liu, Z.; Wu, Y.; Gardner, D. M.; Strutt, N. L.; Cheng, C.; Carmieli, R.; Wasielewski, M. R.; Stoddart, J. F. *Angew. Chem., Int. Ed.* **2013**, *52*, 13100.

(30) Liu, Z.; Liu, G.; Wu, Y.; Cao, D.; Sun, J.; Schneebeli, S. T.; Nassar, M. S.; Mirkin, C. A.; Stoddart, J. F. *J. Am. Chem. Soc.* **2014**, *136*, 16651.

(31) Liu, Z.; Sun, J.; Zhou, Y.; Zhang, Y.; Wu, Y.; Nalluri, S. K. M.; Wang, Y.; Samanta, A.; Mirkin, C. A.; Schatz, G. C.; Stoddart, J. F. *J. Org. Chem.* **2016**, *81*, 2581.

(32) Mizuno, A.; Shuku, Y.; Suizu, R.; Matsushita, M. M.; Tsuchiizu, M.; Reta Mañeru, D.; Illas, F.; Robert, V.; Awaga, K. *J. Am. Chem. Soc.* **2015**, *137*, 7612.

(33) Whittingham, M. S. *Chem. Rev.* **2004**, *104*, 4271.

(34) Armand, M.; Tarascon, J. M. *Nature* **2008**, *451*, 652.

(35) Bruce, P. G.; Scrosati, B.; Tarascon, J.-M. *Angew. Chem., Int. Ed.* **2008**, *47*, 2930.

(36) Goodenough, J. B.; Kim, Y. *Chem. Mater.* **2010**, *22*, 587.

(37) Manthiram, A.; Fu, Y.; Chung, S.-H.; Zu, C.; Su, Y.-S. *Chem. Rev.* **2014**, *114*, 11751.

(38) Tarascon, J. M. *Philos. Trans. R. Soc., A* **2010**, *368*, 3227.

(39) Tobishima, S. i.; Yamaki, J. i.; Yamaji, A. *J. Electrochem. Soc.* **1984**, *131*, 57.

(40) Le Gall, T.; Reiman, K. H.; Grossel, M. C.; Owen, J. R. *J. Power Sources* **2003**, *119*−*121*, 316.

(41) Novák, P.; Müller, K.; Santhanam, K. S. V.; Haas, O. *Chem. Rev.* **1997**, *97*, 207.

(42) Walker, W.; Grugeon, S.; Mentre, O.; Laruelle, S.; Tarascon, J.-M.; Wudl, F. *J. Am. Chem. Soc.* **2010**, *132*, 6517.

(43) Armand, M.; Grugeon, S.; Vezin, H.; Laruelle, S.; Ribiere, P.; Poizot, P.; Tarascon, J. M. *Nat. Mater.* **2009**, *8*, 120.

(44) Song, Z.; Zhou, H. *Energy Environ. Sci.* **2013**, *6*, 2280.

(45) Chen, D.; Avestro, A.-J.; Chen, Z.; Sun, J.; Wang, S.; Xiao, M.; Erno, Z.; Algaradah, M. M.; Nassar, M. S.; Amine, K.; Meng, Y.; Stoddart, J. F. *Adv. Mater.* **2015**, *27*, 2907.

(46) Nishimura, S.-i.; Kobayashi, G.; Ohoyama, K.; Kanno, R.; Yashima, M.; Yamada, A. *Nat. Mater.* **2008**, *7*, 707.

(47) Pasta, M.; Wessells, C. D.; Liu, N.; Nelson, J.; McDowell, M. T.; Huggins, R. A.; Toney, M. F.; Cui, Y. *Nat. Commun.* **2014**, *5*, 3007.

(48) Gawroński, J.; Brzostowska, M.; Gawrońska, K.; Koput, J.; Rychlewska, U.; Skowronek, P.; Nordén, B. *Chem. - Eur. J.* **2002**, *8*, 2484.

(49) Shukla, D.; Nelson, S. F.; Freeman, D. C.; Rajeswaran, M.; Ahearn, W. G.; Meyer, D. M.; Carey, J. T. *Chem. Mater.* **2008**, *20*, 7486.

(50) Gawroński, J.; Brzostowska, M.; Kacprzak, K.; Kołbon, H.; Skowronek, P. *Chirality* **2000**, *12*, 263.

(51) Since the two PMDI protons in (−)-**1PMDI-2NDI-Δ** are homotopic, it is not possible to probe the rate of rotation of the PMDI unit about its C−N···N−C axis by dynamic ^{1}H NMR spectroscopy. Likewise in (−)-**3PMDI-Δ**, the six PMDI protons are homotopic, and so once again it is not possible by dynamic ^{1}H NMR spectroscopy to probe the rate of rotation of the PMDI units about their C−N···N−C axes.

DOI: 10.1021/jacs.6b02086
J. Am. Chem. Soc. 2016, 138, 5968−5977

(52) The significant upfield shifts of the resonances for the heterotopic PMDI protons (H_C and $H_{C'}$) in the ^1H NMR spectra recorded at different temperatures (298−426 K) in CD_3SOCD_3 could be a result of changes in intramolecular shielding effects from neighboring PMDI and NDI units.

(53) The kinetic and thermodynamic parameters associated with the rotation of the PMDI units around the C−N···N−C axis of the isosceles triangle (−)-**2PMDI-1NDI-Δ** were estimated by the peak separation observed ($\Delta\nu_{ex} \approx 11$ Hz) for the PMDI protons (H_C and $H_{C'}$) at low temperatures. The rate constant k_c at the coalescence temperature T_c (426 K) was calculated [Sutherland, I. O. *Annu. Rep. NMR Spectrosc.* **1972**, *4*, 71−235.] employing the approximation that $k_c = \pi(\Delta\nu_{ex})/(2)^{1/2}$ and found to be ∼24 s^{-1}. By using the Eyring equation, $\Delta G_c^{\#} = RT_c \ln(k_c h/k_b T_c)$, in which R is the gas constant, h is Planck's constant, and k_b is Boltzmann's constant, this rate constant (k_c) corresponds to $\Delta G_c^{\#} \approx 23$ kcal mol^{-1}. There is slight line broadening of the signals for the NDI protons ($H_{A/B}$) upon increasing the temperature.

(54) The shape of the CD signal at 380 nm is unsymmetrical on account of the nearby CD signal at 360 nm.

(55) The second set of reduction potentials for [**Ref-PMDI**] and [(−)-**3PMDI-Δ**], corresponding to the generation of [**Ref-PMDI**]$^{2-}$ dianion and [(−)-**3PMDI-Δ**]$^{6-}$ hexaanion, respectively, are too close to that of the solvent (CH_2Cl_2), and hence the second redox potentials could not be accessed.

(56) McConnell, H. M. *J. Chem. Phys.* **1956**, *24*, 764.

(57) A current rate of *n*C refers to achieving full charge or discharge of the battery in 1/*n* h.

(58) The theoretical capacity of each triangle was calculated by assuming a reversible six-electron process under the battery operation conditions.

(59) Gao, J.; Lowe, M. A.; Conte, S.; Burkhardt, S. E.; Abruña, H. D. *Chem. - Eur. J.* **2012**, *18*, 8521.

(60) Shimizu, A.; Kuramoto, H.; Tsujii, Y.; Nokami, T.; Inatomi, Y.; Hojo, N.; Suzuki, H.; Yoshida, J.-i. *J. Power Sources* **2014**, *260*, 211.

(61) Preliminary experiments carried out on the equilateral triangle [(−)-**3PMDI-Δ**] battery revealed that the symmetric nature of [(−)-**3PMDI-Δ**] exhibits, somewhat unexpectedly, improved battery performance. We are currently exploring why this battery does not follow the trend predicted on the basis of the other three batteries.

DOI: 10.1021/jacs.6b02086
J. Am. Chem. Soc. 2016, 138, 5968−5977